

# Phase Transitions, Symmetries, and Tunneling in Parametric Kerr Oscillators

Miguel A. Prado Reynoso,<sup>1</sup> Edson M. Signor,<sup>2</sup> Alexandre D. Ribeiro,<sup>2,3</sup> Francisco Pérez-Bernal,<sup>4</sup> and Lea F. Santos<sup>2</sup>

<sup>1</sup>*Nonlinear Dynamics, Chaos and Complex Systems Group, Departamento de Física, Universidad Rey Juan Carlos, Tulipán s/n, 28933 Móstoles, Madrid, Spain*

<sup>2</sup>*Department of Physics, University of Connecticut, Storrs, Connecticut 06269, USA*

<sup>3</sup>*Departamento de Física, Universidade Federal do Paraná, 81531-990, Curitiba, PR, Brazil*

<sup>4</sup>*Departamento de Ciencias Integradas y Centro de Estudios Avanzados en Física, Matemáticas y Computación, Universidad de Huelva, Huelva 21071, Spain*

We investigate four distinct cases of the parametric Kerr oscillator, a nonlinear quantum system that can be realized in various experimental platforms, including superconducting circuits, exciton-polaritonic systems, and quantum optical cavities. Using a semiclassical Hamiltonian derived within the mean-field approximation, we analyze quantum phase transitions as a function of system parameters. A central focus of our study is the role of rotational symmetry, which allows for the decomposition of the Hamiltonian into irreducible symmetry sectors. This structure plays a crucial role in determining the spectral properties of the system, particularly the emergence of real and avoided crossings in the energy spectrum. By computing the average level spacing within each sector, we identify spectral signatures of avoided crossings that enhance quantum tunneling, as well as real crossings that can suppress tunneling by protecting certain states. Our results highlight the intricate interplay between symmetry, spectral structure, and tunneling dynamics, offering valuable insights for the design and control of quantum states in experimental platforms exhibiting Kerr-type nonlinearities.

## I. INTRODUCTION

Parametric Kerr oscillators (KPOs) have garnered significant attention due to their rich nonlinear quantum dynamics and their potential applications in quantum technologies. These systems can be realized in a variety of experimental platforms, including superconducting circuits, exciton-polaritonic systems, and quantum optical cavities, where they play a crucial role in quantum state engineering, metrology, and information processing. Most studies on KPOs have focused on their role as qubits for quantum computing, particularly in the context of Kerr-cat qubits [? ?] and error-correcting codes [1, 2]. However, recent experimental and theoretical works have begun exploring a broader portion of the spectrum, revealing novel quantum phenomena such as level-kissing events [3] and signatures of excited-state quantum phase transitions (ESQPTs) [4, 5]. Moreover, these systems have been identified as promising quantum simulators for various physical and chemical models [6], further motivating the study of their spectral and dynamical properties.

A fundamental aspect of KPOs is their underlying symmetries, which govern their quantum spectrum and dynamical behavior. Depending on the nature of the nonlinear interaction—whether involving one-, two-, three-, or four-photon squeezing—the Hamiltonian can be decomposed into distinct symmetry sectors. This sectorization strongly influences the appearance of real and avoided crossings in the spectrum, which in turn impacts quantum tunneling. While avoided crossings facilitate tunneling by allowing energy exchange within the same symmetry sector, real crossings between different symmetry sectors can suppress tunneling, effectively protecting certain states from hybridization. These effects are

particularly relevant in the presence of detuning terms, which further enrich the phase diagram of KPOs.

In this work, we systematically investigate the phase diagram of four different effective KPO Hamiltonians, each incorporating a detuning term and one-, two-, three-, or four-photon squeezing interactions. These cases are of current interest and have either been experimentally realized or are expected to be achievable in near-future implementations [7]. Our primary focus is on the characterization of ground-state quantum phase transitions (GSQPTs) and excited-state quantum phase transitions (ESQPTs), which provide key insights into the system's spectral structure and dynamical behavior. GSQPTs are zero-temperature quantum phase transitions driven by quantum fluctuations, characterized by abrupt changes in the ground state when a control parameter crosses a critical value [8]. These transitions are classified according to Ehrenfest's criterion, and although their discontinuous behavior is strictly realized only in the classical limit, clear precursors of their existence can be observed for finite system sizes [9].

Beyond the ground state, the critical points of the system also reveal a second class of phase transitions—ESQPTs—which, in the classical limit, manifest as non-analyticities in the density of states [10–12]. We analyze these transitions in the systems under study and present preliminary results on their influence on tunneling dynamics. By computing the energy spectrum as a function of the detuning parameter, we identify real and avoided crossings, establishing a direct connection between spectral properties and tunneling efficiency. Through an analysis of the average level spacing, we demonstrate that tunneling is maximized when level spacing reaches a minimum and that symmetries can either enhance or inhibit tunneling, depending on the dis-

tribution of avoided and real crossings.

We limit our study to four-photon squeezing interactions, as going beyond this order would result in non-confining potentials due to the quartic character of the Kerr interaction. The consideration of higher-order squeezing terms (five or more photons) would lead to unbounded Hamiltonians, for this cases, symmetries in phase space has been extensively studied in the context of phase-space crystals [13, 14].

Our results provide a deeper understanding of the role of symmetries in nonlinear quantum systems and offer a systematic approach to controlling tunneling dynamics through spectral engineering. These findings have direct implications for experimental platforms where Kerr-type nonlinearities are prominent, paving the way for optimized state control in superconducting circuits, optical lattices, and other quantum devices.

## II. MODEL AND SYMMETRIES

In this section we describe the quantum model and the corresponding classical Hamiltonian, as well as the symmetries of the system.

### A. Quantum Model

In the present paper, we deal with quantum systems described by the effective time-independent Hamiltonian  $\hat{H}_\mu$ , defined as

$$\begin{aligned} \frac{\hat{H}_\mu}{\hbar K} &= \hat{H}_\delta - \xi_\mu (\hat{a}^{\dagger\mu} + \hat{a}^\mu), \\ \hat{H}_\delta &= -\delta (\hat{a}^\dagger \hat{a}) + \hat{a}^{\dagger 2} \hat{a}^2. \end{aligned} \quad (1)$$

Here,  $\hat{H}_\delta$  squeezing independent Hamiltonian operator,  $K$  represents the Kerr nonlinearity,  $\delta \equiv \Delta/K$ , where  $\Delta$  denotes the detuning, and  $\xi_\mu \equiv \epsilon_\mu/K$ , where  $\epsilon_\mu$  is the squeezing amplitude. Our control parameters are  $\delta$  and  $\xi_\mu$ , where the index  $\mu$  takes on the values 1, 2, 3, or 4.

A remarkable feature of model (1), with direct effects to the energy spectrum and dynamics of the system, concerns its symmetries. The Hamiltonian in Eq. (1) commutes with the symmetry operator

$$\hat{s}_\mu \equiv e^{-i2\pi\hat{n}/\mu}, \quad (2)$$

where  $\hat{n} \equiv \hat{a}^\dagger \hat{a}$  is the number operator. Notice that the Fock states  $|n\rangle$  are eigenstates of the symmetry operator, that is,  $\hat{s}_\mu |n\rangle = e^{-i2\pi n/\mu} |n\rangle$ , having only  $\mu$  distinct eigenvalues. This implies that the eigenstates of the Hamiltonian are superpositions of Fock states sharing the same symmetry eigenvalue. Consequently, the Hilbert space of the system is partitioned into  $\mu$  invariant sectors, each associated with a distinct eigenvalue of  $\hat{s}_\mu$ . By invariance, we mean that an initial state spanned exclusively by the eigenstates with the same symmetry eigenvalue will evolve, under the action of  $\hat{H}$ , to states spanned

by the same set of eigenstates. One can easily verify that the present discussion is trivial for the case  $\mu = 1$ , as  $\hat{s}_1$  is the identity operator. Furthermore, for  $\mu = 2$  the symmetry operator  $\hat{s}_2$  simplifies to the well-known parity operator  $\hat{P} \equiv (-1)^{\hat{n}}$ .

To formalize these ideas, we define  $\mu$  distinct basis  $\mathcal{B}_k^\mu \equiv \{|b_k^j\rangle\}$ , for  $k = 0, 1, \dots, \mu - 1$ , composed of the Fock states. The  $j$ -th element of basis spanning  $k$ -sector is  $|b_k^j\rangle = |k + \mu j\rangle$ , for  $j = 0, 1, \dots$ . Then, an eigenstate of  $\hat{H}$ , assigned to the  $k$ -sector, can be expressed by the expansion

$$|E_k^i\rangle = \sum_{j=0}^{\infty} d_k^{i,j} |b_k^j\rangle, \quad (3)$$

with coefficients  $d_k^{i,j}$ . The label  $E_k^i$  represents the  $i$ -th energy eigenvalue of the  $k$ -sector.

These concepts of symmetry sectors are essential for understanding the behavior of the energy spectrum as a function of the Hamiltonian parameters. According to the Wigner–Neumann theorem [15, 16], real degenerate energy eigenvalues correspond to eigenstates from different symmetry sectors, whereas quasidegenerate energy levels (associated with avoided crossings) occur within the same symmetry sector. The Hamiltonian (1) is also invariant under time-reversal and reflection symmetries. However, these symmetries are anti-unitary [referencias?], which implies that the Hamiltonian cannot be decomposed into additional irreducible sectors associated with them.

### B. Classical Hamiltonian

By analyzing the classical limit of the system, we can determine the critical points, assess their stability, and calculate their associated energies, which allows us to construct phase diagrams. The classical Hamiltonian, derived in the Appendix A, is expressed as follows:

$$\begin{aligned} \frac{H_\mu^c}{K} &= H_\delta^c - \frac{2\xi_\mu}{2^{\mu/2}} \mathcal{F}_\mu, \\ H_\delta^c &= -\frac{\delta}{2} (q^2 + p^2) + \frac{1}{4} (q^2 + p^2)^2 \end{aligned} \quad (4)$$

where we have defined  $\mathcal{F}_\mu \equiv \text{Re}[(q+ip)^\mu]$ , so that  $\mathcal{F}_1 = q$ ,  $\mathcal{F}_2 = q^2 - p^2$ ,  $\mathcal{F}_3 = q^3 - 3qp^2$  and  $\mathcal{F}_4 = q^4 - 6q^2p^2 + p^4$ . The squeezing independent classical Hamiltonian is given by  $H_\delta^c$ .

Symmetries are also present in the classical model in Eq.(4). They can be seen in the phase-space structure of each  $\mu$ -system. In fact, they manifest as invariant rotations around the phase-space origin. To show it, consider the complex variable  $z = |z|e^{i\theta}$  and its complex conjugate  $z^*$  such that  $z = q + ip$ . In terms of these new variables, the Hamiltonian function (4) becomes  $H_\mu^z = -\frac{\delta}{2}|z|^2 + \frac{1}{4}|z|^4 - \frac{\xi_\mu}{2}(z^\mu + z^{*\mu})$ . Rotating the phase-space surface  $H_\mu^z$  by an angle  $\beta$  around the origin

corresponds to changing variable  $z$  as  $z \rightarrow z e^{-i\beta}$ . Notice that  $H_\mu^z$  becomes invariant if one assumes  $\beta = 2\pi/\mu$ . Therefore, whatever the phase-space structure of  $H_\mu^c$ , it will surely manifest a symmetry with respect to a  $(2\pi/\mu)$ -rotation around the origin.

### III. CLASSICAL AND QUANTUM PHASE TRANSITIONS

We analyze phase transitions using semiclassical methods applied to phase space, bridging classical and quantum dynamics. By examining phase-space evolution as system parameters vary, we identify critical points, bifurcations, and new dynamical regions. In classical Hamiltonian systems, stationary points play a key role in shaping both dynamics and phase-space structure. As parameters change, the positions, energy values, and stability of these points evolve, leading to transitions characterized by the emergence or disappearance of separatrices that define distinct dynamical regions.

These methods reveal the underlying topology of the classical system and provide geometric insights into quantum phase transitions (QPTs) and excited-state quantum phase transitions (ESQPTs). In the quantum regime, these transitions manifest as changes in the energy spectrum, often associated with degenerate or quasi-degenerate eigenvalues. Such spectral changes emphasize the deep connection between classical and quantum descriptions of the system.

#### 1. Ground state phase transitions: order parameter

The order parameter is a fundamental physical quantity that characterizes quantum phase transitions (QPTs) in the ground state. It is defined as a property of the system that undergoes a qualitative or quantitative change upon crossing the critical point, reflecting a structural transformation in the system's phase.

In first-order transitions, the order parameter typically exhibits a discontinuous change, whereas in second-order transitions, it changes continuously but with singularities in its derivatives. Its definition depends on the relevant physical observable of the system and is measured by analyzing its dependence on the control parameter. Near the critical point, the order parameter captures the critical properties of the system, serving as a key tool for describing and analyzing the nature of quantum phase transitions.

In this work, a suitable order parameter is defined as the derivative of the ground state energy with respect to the detuning  $\delta$  or the corresponding squeezing  $\xi_\mu$ . Consequently, any classical bifurcation induced by both variations in these parameters is captured by the operator, which also allows for a straightforward computation in both classical and quantum systems (see Appendix B for further details).

#### 2. Density of states and excited states QPT

Analyzing the classical and quantum densities of states (CDOS and QDOS) provides critical insights into phase transitions by illustrating how states are distributed across energy levels. The CDOS, defined as the phase space volume at a given energy, and the QDOS, representing the number of eigenstates per energy interval, are connected through semiclassical approximations:

$$\rho(\mathcal{E}) = \frac{1}{2\pi} \int dq dp \delta(H_{cl} - \mathcal{E}), \quad (5)$$

where  $\rho(\mathcal{E})$  is the classical density of states. At large quantum numbers, the QDOS converges to the CDOS, with quantum corrections capturing finer dynamical details [17].

Classical phase transitions are marked by discontinuities or non-analytic behaviors in the CDOS, reflecting changes in the topology of phase space. Similarly, quantum phase transitions, including excited-state quantum phase transitions, exhibit abrupt changes in the QDOS. Comparing CDOS and QDOS provides a means to trace the classical origins of quantum transitions and their interplay.

In the following, we present a systematic analysis of the phase space and phase diagram for each classical  $\mu$ -system, exploring their connection to quantum phase transitions and excited-state quantum phase transitions. Due to the symmetry of the system with respect to the squeezing parameter  $\xi_n$ , the transitions for a positive value are analogous to those for a negative value. For this reason, it is sufficient to analyze the phase transitions for  $\xi_n \geq 0$ .

The stationary (critical) points of a classical Hamiltonian system described by Eq. (4) are identified through Hamilton's equations of motion, which define the conditions for equilibrium in the system.

$$\begin{aligned} \dot{q} &= -p [\delta - (q^2 + p^2)] + \frac{2\xi_\mu^c}{2^{\mu/2}} \left( \frac{\partial \mathcal{F}_\mu}{\partial p} \right), \\ \dot{p} &= q [\delta - (q^2 + p^2)] - \frac{2\xi_\mu^c}{2^{\mu/2}} \left( \frac{\partial \mathcal{F}_\mu}{\partial q} \right). \end{aligned} \quad (6)$$

#### A. One-photon squeezing $\xi_1$ and detuning $\delta$

The first case corresponds to the classical Hamiltonian,

$$H_1^c = H_\delta^c - \sqrt{2}\xi_1 q. \quad (7)$$

When  $\mu = 1$ , a straightforward inspection of Eq. (6) shows that all critical points have zero momentum. Nonetheless, finding the stationary position requires solving the cubic equation  $q_s^3 - \delta q_s - \sqrt{2}\xi_1 = 0$ . The behavior of this equation is determined by its discriminant,  $\delta_{dsc} \equiv 4\delta^3 - 54\xi_1^2$ . When  $\delta_{dsc} < 0$ , the equation admits three distinct real solutions, while for  $\delta_{dsc} \geq 0$ , it has only

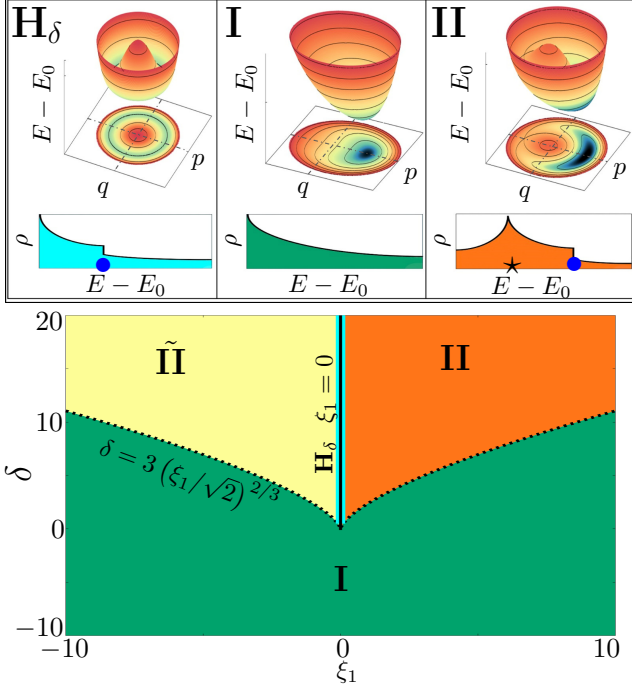


FIG. 1. One-photon squeezing case. Top panels: Classical quasipotential, phase space structure, and sketches of the density of states for phases  $H_\delta$ , I, and II. Bottom panel: Phase diagram for the detuning parameter  $\delta$  and the one-photon squeezing amplitude  $\xi_1$ . Ground-state quantum phase transition is represented by a solid line, while excited-state quantum phase transitions are indicated by dashed lines.

one real solution. Thus, the parameter space is settled from the discriminant in Fig.1.

In Case I, for  $\{\delta \leq 3(\xi_1/\sqrt{2})^{2/3}\}$ , only a single stationary point exists (upper middle panel of Fig.1). This point corresponds to a stable global minimum. In this regime, the phase space is characterized by a simple single-well configuration, and the density of states (DOS) decreases monotonically with increasing energy.

As the parameter increases, for  $\{\delta > 3(\xi_1/\sqrt{2})^{2/3}\} \cap \{\xi_1 = 0\}$ , the system transitions to a more complex regime, where the cubic equation admits three stationary points. These include a stable equilibrium point corresponding to the energy minimum, unstable hyperbolic points that create separatrices in the phase space and divide it into distinct dynamical regions, and a local maximum representing the highest energy stationary point.

The transition at  $\delta = 3(\xi_1/\sqrt{2})^{2/3}$  represents a critical threshold where the system undergoes significant structural changes in both the energy landscape and the phase-space topology. In the single-well regime (Case I), the DOS remains smooth and monotonic. In contrast, in the case II, the DOS becomes more complex, with critical divergences and step-like behavior corresponding to the new stationary points at higher energy. These critical

energy features are direct signatures of two excited-state quantum phase transitions (ESQPTs), one logarithmic divergence ESQPT associated with the hyperbolic point, and the other, a step ESQPT, associated with local maximum.

A transition in the stability of the critical point of the global minima occurs when a crossing in the parameters takes place at  $\{\delta > 0\} \cap \{\xi_1 = 0\}$  (cyan line Fig.1). Specifically, from regions II to region IĨ, or vice versa. This shift in the global minimum is a hallmark of a quantum phase transition (QPT).

When the Density of States (DOS) is plotted at this transition (blue curve in the leftmost upper panel), a monotonic decrease with a step-like feature indicates a first-order transition (see the Appendix B for details on the order parameter). In all parameter diagrams, solid white lines between the transition regions highlight the quantum phase transitions, while the dotted lines indicate the quantum phase transitions of excited states.

## B. Two-photon squeezing $\xi_2$ and detuning $\delta$

For  $\mu = 2$ , the corresponding classical Hamiltonian is given by

$$H_2^c = H_\delta^c - \xi_2 (q^2 - p^2). \quad (8)$$

Solving the system of equations (6) for  $\mu = 2$ , we distinguish five critical points  $r = \{q, p\}$ , which are listed below together with their corresponding energy  $\mathcal{E}$ :

$$\begin{aligned} r_0 &= \{0, 0\}, & \mathcal{E}_{r_0} &= 0, \\ r_1^\pm &= \left\{ 0, \pm \sqrt{\delta - 2\xi_2} \right\}, & \mathcal{E}_{r_1^\pm} &= - \left( \frac{\delta - 2\xi_2}{2} \right)^2, \\ r_2^\pm &= \left\{ \pm \sqrt{\delta + 2\xi_2}, 0 \right\}, & \mathcal{E}_{r_2^\pm} &= - \left( \frac{\delta + 2\xi_2}{2} \right)^2. \end{aligned} \quad (9)$$

By analyzing the stability of these points, we identify the following three scenarios in Fig.2 [? ? ].

For Case (2.I), corresponding to  $\delta \leq -2\xi_2$ , there is only one stationary point at  $r_0$ , as shown in the phase-space diagram. This point is stable and represents a global minimum. The density of states decreases monotonically as the energy increases, indicating a simple and stable dynamical structure.

Case (2.II): For  $-2\xi_2 < \delta \leq 2\xi_2$ , there are three stationary points, as shown in the phase-space diagram. Two of them are stable points at  $r_2^\pm$ , which are global minima, and  $r_0$  now becomes an unstable hyperbolic point. This change is clearly visible in the corresponding phase-space diagram.

Case (2.III): For  $\{\delta > 2\xi_2\} \cap \{\xi_2 = 0\}$ , there are five stationary points, as shown in the phase-space diagram. These are the same two stable global minima at  $r_2^\pm$  as in Case (II), there are also two unstable hyperbolic points

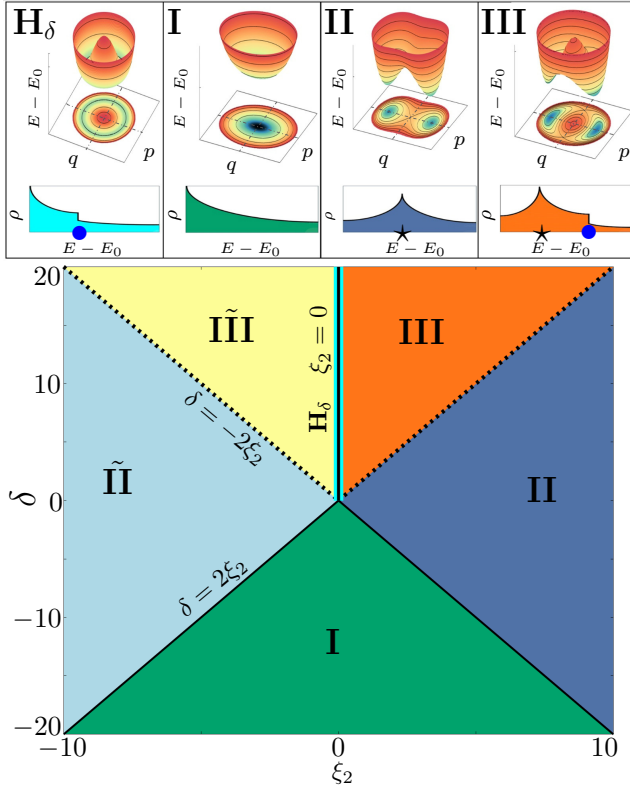


FIG. 2. Two-photon squeezing case. Top panels: Classical quasipotential, phase space structure, and sketches of the density of states for phases  $H_\delta$ , I,II, and III. Bottom panel: Phase diagram for the detuning parameter  $\delta$  and the one-photon squeezing amplitude  $\xi_2$ . Ground-state quantum phase transition is represented by a solid line, while excited-state quantum phase transitions are indicated by dashed lines.

at  $r_1^\pm$ , and  $r_0$  recover their status of a stable point, as in Case (I), though now it is a local maximum.

From these results, the phase-space structure of  $H_2^c$  is completely determined as illustrated in Fig. 2. In the lower panel, we show the phase diagram of  $H_2^c$  in the parameter space, highlighting the transitions between the different cases.

The transition from Case (2.I) to Case (2.II) marks the occurrence of both a quantum phase transition (QPT) and an excited-state quantum phase transition (ESQPT). During this process, the single minimum at the origin bifurcates into two new stationary points,  $r_2^\pm$ , which become stable global minima. This bifurcation results in a second-order QPT (see the Appendix B for details on the order parameter). As one crosses the region I, the original stationary point at  $r_0$  transforms into a hyperbolic point, generating a logarithmic-type ESQPT.

In contrast, the transition from Case (2.II) to Case (2.III) involves only an ESQPT. This transition originates from the bifurcation of the existing hyperbolic point into three new points: a stable point at the origin with energy  $E = 0$ , and two new hyperbolic points with intermediate negative energies. The ESQPT associated

with the stable point at the origin is of the step-like type, while the hyperbolic points give rise to a logarithmic-type ESQPT.

Finally, similar to the  $\mu = 1$  parameter diagram, Case III can be mapped onto its mirrored counterpart,  $\tilde{III}$ , leading to a QPT between them. This transition is characterized by a step-like feature in the DOS and exhibits first-order behavior.

### C. Three-photon squeezing $\xi_3$ and detuning $\delta$

We now turn to the phase-space structure of  $H_3^c$  given by

$$H_3^c = H_\delta^c - \frac{\xi_3}{\sqrt{2}} (q^3 - 3qp^2). \quad (10)$$

By applying Eq. (6) to this system, we identify the existence of the following seven stationary points, each associated with its corresponding energy:

$$\begin{aligned} \mathbf{r}_0 &= \{0, 0\}, & \mathcal{E}_{r_0} &= 0 \\ \mathbf{r}_1^\pm &= \left\{ Q_\pm, 0 \right\}, & \mathcal{E}_{r_1^\pm} &= \mathcal{E}_\pm \\ \mathbf{r}_2^\pm &= \left\{ -\frac{1}{2}Q_+, \pm \frac{\sqrt{3}}{2}|Q_\pm| \right\}, & \mathcal{E}_{r_2^\pm} &= 0 \\ \mathbf{r}_3^\pm &= \left\{ -\frac{1}{2}Q_-, \pm \frac{\sqrt{3}}{2}|Q_\pm| \right\}, & \mathcal{E}_{r_3^\pm} &= 0. \end{aligned} \quad (11)$$

where  $Q_\pm = (3\xi_3 \pm \sqrt{9\xi_3^2 + 8\Delta}) / 2\sqrt{2}$  and  $\mathcal{E}_\pm = \text{Give energies, ... 1st order}$ . Fig. 3 exhibits the energy contours and the phase diagram for  $\mu = 3$ .

For  $\delta \leq -9\xi_3^2/8$ , Case 3.I, the system features a single stationary point located at  $r_0$ , which is stable and serves as the global minimum. The phase-space topology is simple, and the density of states (DOS) decreases monotonically as the energy increases.

As the parameter increases in the region  $\{\delta < -\xi_3^2\} \cap \{\delta < -9\xi_3^2/8\}$ , we have Case 3.II. Six new stationary points emerge. The global minimum remains at the origin, but the new stationary points are distributed across two distinct energy levels: three hyperbolic points at the same energy corresponding to local maxima, and three local minima forming three identical potential wells. This structural change in phase space introduces two distinct types of ESQPTs: a logarithmic ESQPT at the energy of the hyperbolic points and a step-like ESQPT associated with the local minima. These transitions result in significant changes in DOS, with logarithmic divergences and step-like increases appearing at the respective critical energy levels.

At  $\delta = -\xi_3^2$ , case III, the system retains the seven stationary points from Case II, but their energies shift. The energy of the local minima decreases until it matches the energy of the origin, creating a degenerate configuration where the origin and the three local minima share the

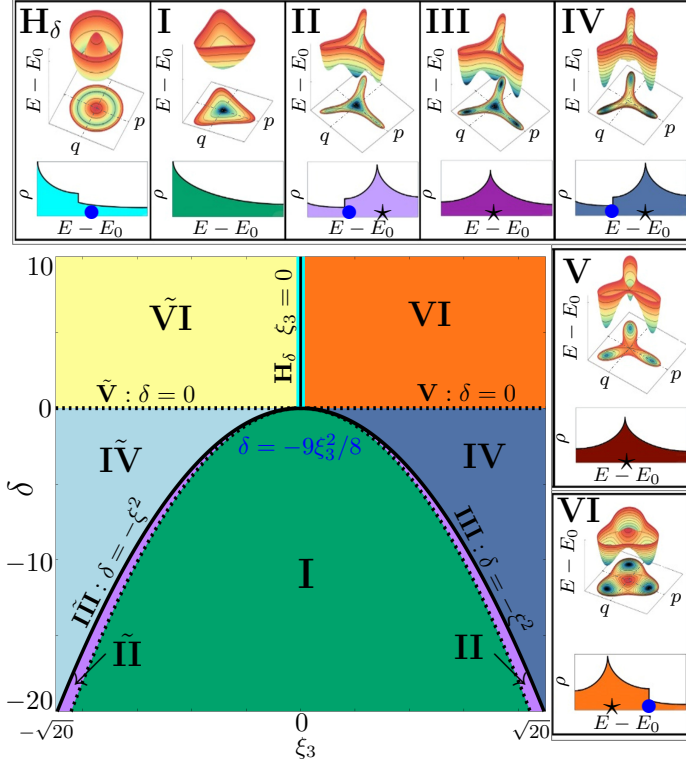


FIG. 3. Three-photon squeezing case. Top panels: Classical quasipotential, phase space structure, and sketches of the density of states for phases  $H_\delta$  and I-VI. Bottom panel: Phase diagram for the detuning parameter  $\delta$  and the one-photon squeezing amplitude  $\xi_3$ . Ground-state quantum phase transition is represented by a solid line, while excited-state quantum phase transitions are indicated by dashed lines.

same energy. This marks a QPT, indicating a fundamental change in the system's global configuration. The observed feature is characteristic of a first-order transition. Due to this degeneration, the density of states (DOS) no longer exhibits the step-like ESQPT, while the logarithmic ESQPT associated with the hyperbolic points remains.

In the range  $\{\delta < 0\} \cap \{\delta \leq -\xi_3^2\}$ , case IV, the energy of the hyperbolic points continues to decrease, remaining positive, while the origin transitions from a global minimum to a local minimum. Simultaneously, the energy of the three external minima decreases further, becoming the new global minima. This rearrangement in the energy landscape is evident in the DOS, which features a pronounced logarithmic divergence near the hyperbolic points and step-like features at the deeper global minima.

For  $\delta = 0$ , case V, the three hyperbolic points converge at the origin, transforming it into a hyperbolic point and reducing the total number of stationary points to four. The three global minima deepen further as their energies decrease, resulting in increasingly pronounced potential wells. The DOS captures these transitions, with the logarithmic divergence now centered at the energy of

the origin, reflecting the profound reorganization of the phase-space topology.

Finally, for  $\{\delta > 0\} \cap \{\xi_3 = 0\}$ , case VI, the stationary point at the origin persists, transitioning into a stable local maximum. Three hyperbolic points bifurcate from the origin, while the three global minima continue to decrease in energy, further deepening their respective wells. The DOS evolves accordingly, displaying logarithmic divergences at hyperbolic points and step-like increases associated with increasingly dominant global minima.

#### D. Four-photon squeezing $\xi_4$ and detuning $\delta$

Finally, we will deal with the classical description of the case  $\mu = 4$ .

$$H_4^c = H_\delta^c - \frac{\xi_4}{2} (q^4 - 6q^2p^2 + p^4). \quad (12)$$

A straightforward analysis of the classical Hamiltonian (4) indicates that the nonlinear parameter must satisfy  $\xi_4 < 1/2$ ; otherwise,  $H_4^c$  becomes unbounded. Specifically, as  $\xi_4 \rightarrow 1/2$ , the Hamiltonian asymptotically approaches  $-q^2p^2$ , which is not confined. In this regime, the quantum energy spectrum becomes negative and continuous. By solving the system of equations (6) for  $\mu = 4$ , we identify nine critical points. These points, along with their corresponding energies  $\mathcal{E}$ , are listed below:

$$\begin{aligned} \mathbf{r}_0 &= \{0, 0\}, & \mathcal{E}_{\mathbf{r}_0} &= 0 \\ \mathbf{r}_1^\pm &= \left\{ 0, \pm\sqrt{Q_a} \right\}, & \mathcal{E}_{\mathbf{r}_1} &= -Q_a^2/4 \\ \mathbf{r}_2^\pm &= \left\{ \pm\sqrt{Q_a}, 0 \right\}, & \mathcal{E}_{\mathbf{r}_2} &= -Q_a^2/4 \\ \mathbf{r}_{3,4}^\pm &= \left\{ \pm\sqrt{Q_d}, \pm\sqrt{Q_d} \right\}, & \mathcal{E}_{\mathbf{r}_{3,4}} &= -Q_d^2. \end{aligned} \quad (13)$$

where  $Q_a = \delta/(1 - 2\xi_4)$  and  $Q_d = \delta/[2(1 + 2\xi_4)]$ . Essentially, two distinct phase-space structures may emerge depending on the parameters  $\delta$  and  $\xi_4$  leading to Fig.4. The first, Case I, corresponds to  $\delta \leq 0$ , there is only one stationary point at  $r_0$ , as shown in the phase-space diagram. This stable point is a global minimum.

In case II, For  $\{\delta > 0\} \cap \{\xi_4 = 0\}$ , the phase space structure become more complex. The stationary point at the origin transitions into a maximum while retaining its energy. Concurrently, eight new stationary points bifurcate from it: four of these points, which share the same energy, correspond to global minima and define four equivalent potential wells. The remaining four points, with intermediate energy, are hyperbolic, introducing regions of instability into the phase space. These configurations are depicted in the phase-space diagram.

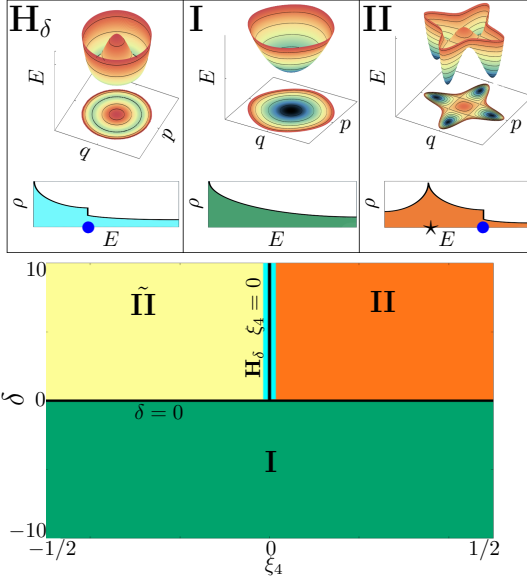


FIG. 4. Four-photon squeezing case. Top panels: Classical quasipotential, phase space structure, and sketches of the density of states for phases  $H_\delta$ , I, and II. Bottom panel: Phase diagram for the detuning parameter  $\delta$  and the one-photon squeezing amplitude  $\xi_4$ . Ground-state quantum phase transition is represented by a solid line, while excited-state quantum phase transitions are indicated by dashed lines.

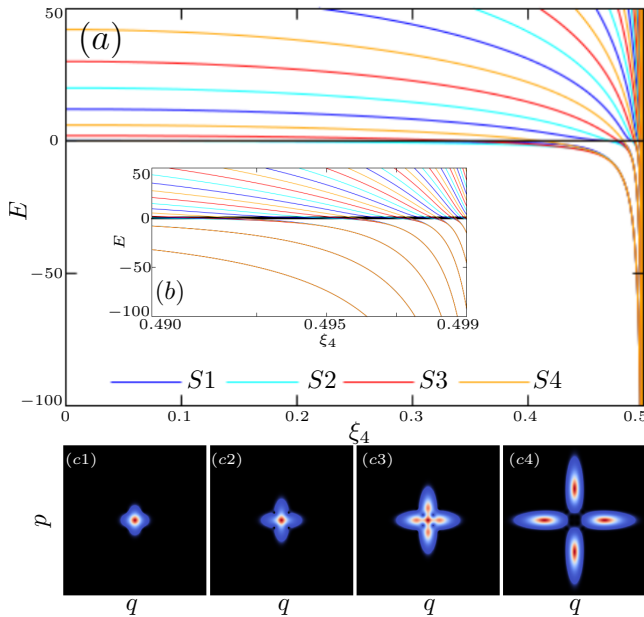


FIG. 5. Energy as a function of the squeezing parameter  $\xi_4$  for  $\delta = 0$ , each color represents an irreducible block. As  $\xi_4 \rightarrow 1/2$ , a quasi-degeneracy emerges, associated with the four symmetries of the system, effectively behaving as four equivalent wells (zoom in panel b). In contrast, this transition is not observed in the classical description. [Missing discussion plots C1, ..., C4](#)

### 1. When the transition is only quantum

Before concluding this discussion about the phase-space structure, it is important to emphasize that the analysis presented is based on semiclassical methods [usando campo medio/estados coherentes?](#). This reliance on semiclassical approximations may lead to certain limitations. For instance, there are scenarios where the classical Hamiltonian cannot predict a quantum phase transition that arises solely in the quantum regime.

While semiclassical methods provide valuable insights by bridging these two regimes, they may not fully capture all phenomena inherent to the quantum domain. Consequently, caution is necessary when interpreting phase transitions based solely on classical or semiclassical analyses, as certain quantum effects could remain hidden without a fully quantum treatment.

This behavior occurs in the  $\delta$ -Kerr  $\xi_4$ -model. In Fig.5, the quantum energy levels are plotted as a function of the squeezing parameter, considering a detuning parameter of zero. Classically, as shown in Fig.4, there is no associated phase transition in this case. Classical intuition suggests the system should remain non-degenerate, with no negative energy values.

However, a direct diagonalization of the quantum Hamiltonian reveals a different picture. As  $\xi_4 \rightarrow 1/2$ , the energy levels gradually decrease, eventually reaching negative values. Moreover, energy levels from different symmetry sectors become degenerate in groups of four, as if an effective four-well potential were emerging.

This result underscores the limitations of purely classical analysis in capturing quantum effects and highlights how quantum mechanics can reveal new structural features, such as symmetry-induced degeneracies, that are not apparent in the classical phase-space description.

## IV. QUANTUM TUNNELING

Quasi-degenerate energy levels within the same symmetry sector indicate strong interactions that enhance the tunneling process. Identifying such regions in parameter space is crucial for applications where tunneling plays a fundamental role, such as quantum transport, coherent state manipulation, and the design of advanced quantum devices. Conversely, understanding these regions is also essential for protecting tunneling states through the symmetries of the system.

In this section, we explore the dynamical implications of level crossings within each symmetry sector, focusing specifically on the tunneling phenomenon. Tunneling refers to the quantum mechanical transition of an initial state between classically forbidden regions of phase space. As demonstrated in [5], quasi-degeneracies within the same symmetry sector facilitate this process. Building upon this observation, we employ level spacing as a diagnostic tool to identify the optimal parameters for maximizing tunneling. By analyzing the energy spec-

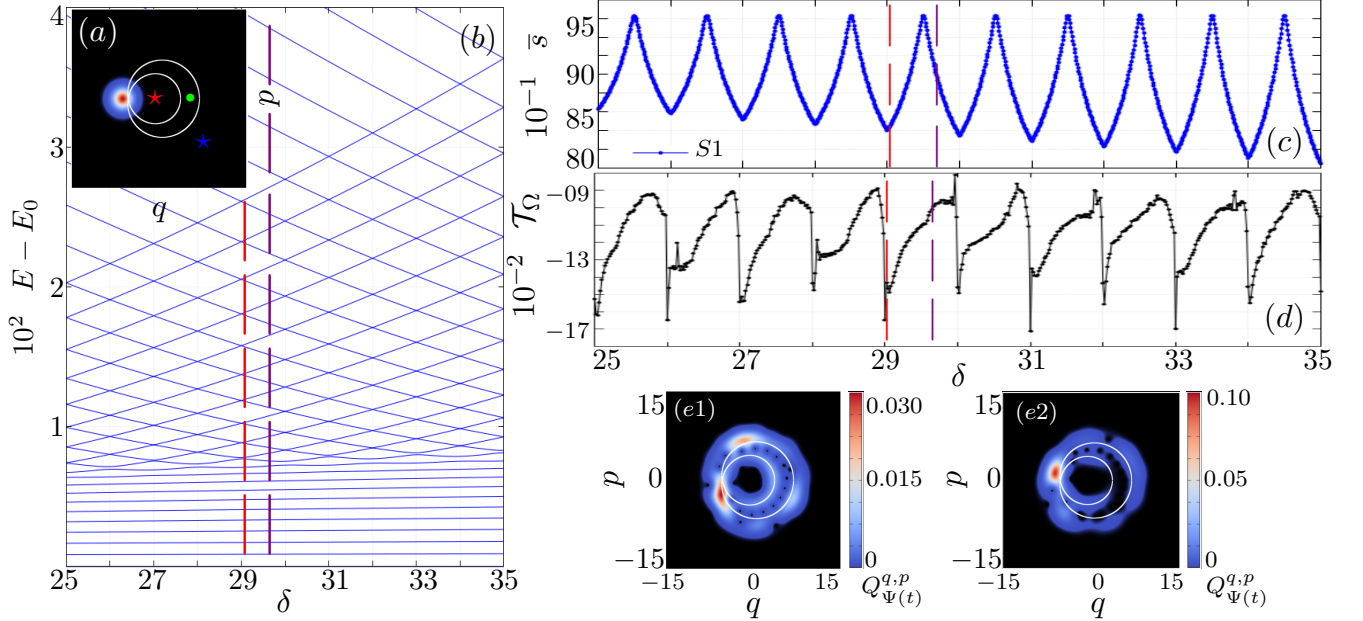


FIG. 6. Tunneling in the  $\delta$ -Kerr  $\xi_1$ -model as a function of the detuning parameter. (a) Excitation energy. (b) Average level spacing for the first 150 levels. (c) Effective tunneling. (d1) Initial state and its time evolution at  $t = 100$  for (d2)  $\delta = 29.05$  and (d3)  $\delta = 29.75$

trum, we pinpoint regions where the spacing between adjacent energy levels are minimal — a signature of enhanced tunneling dynamics.

To quantify tunneling, we require a measure that captures how the evolved quantum state explores specific regions of phase space. For this purpose, we employ the Husimi function in the position and momentum representation, computed for the time-evolved state  $|\Psi(t)\rangle = e^{-i\hat{H}t}|\Psi(0)\rangle$ , as follow

$$\mathcal{Q}_{\Psi(t)}^{(q,p)} = \frac{1}{\pi} |\langle \alpha(q,p) | \Psi(t) \rangle|^2, \quad (14)$$

where  $\mathcal{Q}_{\Psi(t)}^{(q,p)}$  provides a quasi-probability distribution over phase space. To study tunneling dynamics, we define and analyze specific invariant regions of phase space, denoted as  $\Omega$ , that remain unchanged under classical evolution. A region  $\Omega \subset \mathcal{M}$  is considered invariant if, for any initial condition  $x \in \Omega$ , the classical trajectory remains confined to  $\Omega$  for all times  $t$ , i.e.,  $\varphi_x(t) \in \Omega$ , where  $\varphi : \mathbb{R} \times \mathcal{M} \rightarrow \mathcal{M}$  represents the flow defined by Hamilton's equations of motion in Eq. (6).

For a given invariant region  $\Omega \subset \mathcal{M}$ , we define the *Husimi volume* at time  $t$  as [?]:

$$\mathcal{V}_\Omega(t) = \iint_{\Omega_k} dq dp \mathcal{Q}_{\Psi(t)}^{(q,p)}, \quad (15)$$

which quantifies the portion of the quantum state localized within  $\Omega$ . The Husimi volume is normalized such

that  $\mathcal{V} = 1$  when the integral is performed over the entire phase space,  $\Omega = \mathcal{M}$ . This computation is efficiently performed using Monte Carlo integration methods [?].

To quantify tunneling dynamics, we introduce the concept of *effective tunneling*, defined as the change in Husimi volume within a region  $\Omega$  over a time interval  $[t_0, t]$ :

$$\mathcal{T}_\Omega(t, t_0) = \mathcal{V}_\Omega(t) - \mathcal{V}_\Omega(t_0). \quad (16)$$

This measure captures the net flow of the quantum state in or out of the region  $\Omega$  during the specified time period, providing a clear and quantitative way to analyze tunneling phenomena in the system. We analyze each case in detail.

### A. Tunneling in the Absence of Irreducible Symmetries

We begin the study of tunneling for the case where the system lacks rotational symmetry, specifically for Case  $\mu = 1$ . This implies that the Hamiltonian cannot be decomposed into irreducible sectors, and as a result, the system does not exhibit real crossings.

#### 1. Tunneling for $\delta$ -Kerr $\xi_1$ -model

For the one-photon squeezing system, we focus on Case II in Fig. 1. The classical phase space features a global minimum, a local maximum, and a hyperbolic point, as

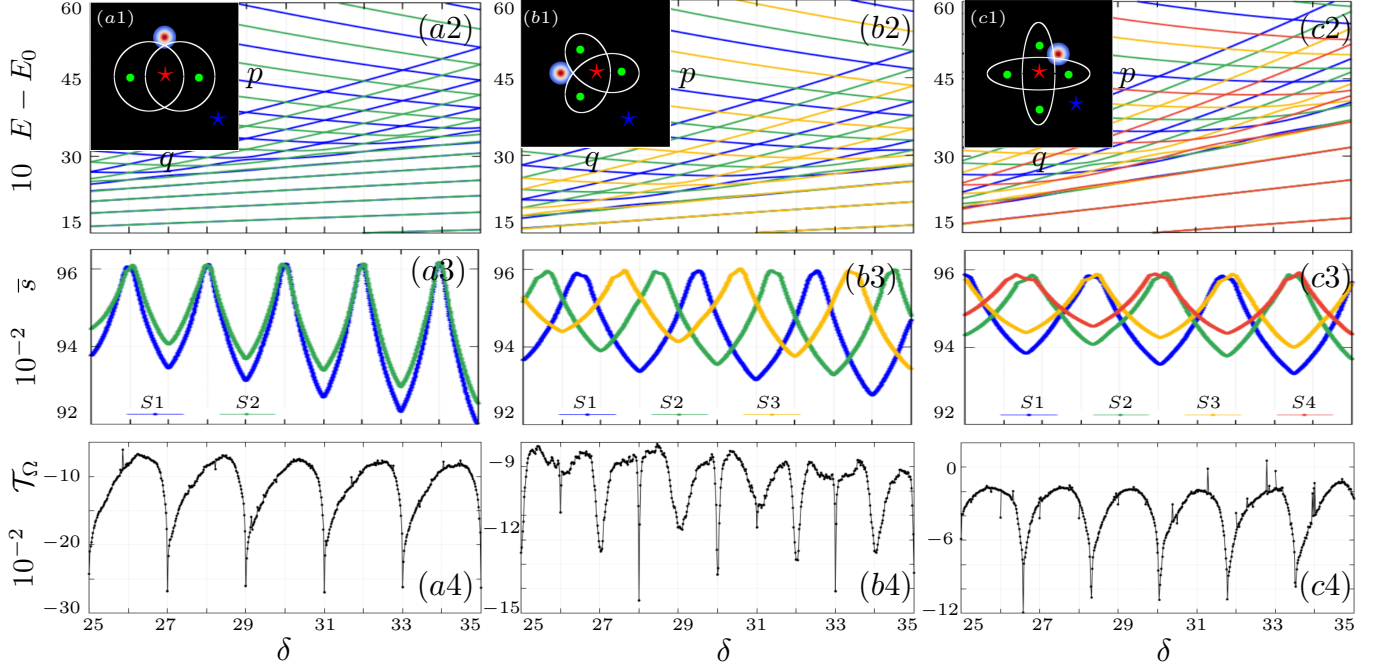


FIG. 7. Level spacing for each symmetry as a function of the detuning parameter  $\delta$ . For each case, 150 energy levels were considered. Cuando solo hay cruces reales entre las simetrías, la media del level spacing es similar en todas las simetrías

shown in Fig. 6(a1). The separatrix (depicted in white) delineates the distinct classical phase-space regions. Trajectories within the region marked by a star, and with energy between the hyperbolic point and the local maximum, are degenerate in pairs—meaning that two distinct trajectories share the same energy.

In Fig. 6(b), we compute the spectrum of the Hamiltonian in Eq.(7) as a function of the detuning parameter, fixing  $\xi_1 = 5$ . For low energies, below the logarithmic ES-QPT (associated with the hyperbolic point), and for high energies, beyond the step-like ESQPT (associated with the local maximum), the spectrum is non-degenerate. In contrast, in the intermediate region, the spectrum exhibits avoided crossings for certain values of the detuning parameter. The absence of real crossings is a consequence of the fact that the Hamiltonian lacks symmetries that can decompose it into independent sectors.

In Fig. 6(c), we compute the average level spacing for the same parameters used in Fig. 6(b). The analysis is performed over a spectral region extending beyond the ESQPTs, up to energies exceeding the step-like ESQPT. As expected, the minima in the level-spacing distribution align with the energy values at which avoided crossings occur, indicating resonant coupling between quasi-degenerate states.

To probe the quantum tunneling dynamics, we compute the effective tunneling for an initial coherent state with energy slightly above the logarithmic ESQPT, localized near the hyperbolic point, as depicted in Fig. 6(a). The tunneling results, presented in Fig. 6(d), reveal a clear correlation between the minima in the level-spacing

distribution and the enhancement of tunneling. This correspondence underscores the role of avoided crossings in the phenomenon of quantum tunneling.

Additionally, Fig. 6(e1)-(e2) shows the Husimi functions of the evolved states after a time  $t = 100$ . In Fig. 6(e2), corresponding to the parameter  $\delta = 29.05$ , where the level spacing is minimal, we observe increased tunneling toward the central region. In contrast, in Fig. 6(e2), with  $\delta = 29.754$ , the level spacing is larger, and tunneling toward the central region is reduced. In both cases, we also observe that part of the state escapes towards the lower energy region in the form of a crescent.

## B. Tunneling with Irreducible Symmetries

In this section, we focus on the study of tunneling in systems that can be decomposed into irreducible sectors due to rotational symmetry. We will examine cases with two, three, and four symmetries, corresponding to the two-photon, three-photon, and four-photon squeezing systems, respectively.

For the  $\delta$ -Kerr  $\xi_2$  model, we focus on Case III, as shown in Fig. 2; for the  $\delta$ -Kerr  $\xi_3$  model, we focus on Case VI in Fig. 3; and for the  $\delta$ -Kerr  $\xi_4$  model, we focus on Case II in Fig. 4. The classical phase space exhibits  $\mu = 2, 3, 4$  global minima, a local maximum, and  $\mu = 2, 3, 4$  hyperbolic points, as shown in Fig. 7(a1), Fig. 7(b1), and Fig. 7(c1), respectively. Similar to the case  $\mu = 1$ , trajectories within the region marked by a star, and with energy between the hyperbolic points and the local maximum,

are degenerate in pairs—meaning two distinct trajectories share the same energy. Additionally, for each case, the lower-energy regions marked with green circles also correspond to trajectories with the same energy, generating  $\mu = 2, 3, 4$  distinct trajectories sharing the same energy.

### 1. Tunneling for $\delta$ -Kerr $\xi_2$ -model

For the two-photon squeezing system, we fix  $\xi_2 = 5$  and compute the spectrum of the Hamiltonian in Eq. (7) as a function of the detuning parameter, as shown in Fig. 7(a2). In this case, the Hamiltonian can be decomposed into two symmetry sectors, with each color representing a different sector. We observe that the spectrum is degenerate and exhibits both real and avoided crossings for certain values of the detuning parameter. The real crossings occur between states belonging to different symmetry sectors, while the avoided crossings appear within the same symmetry sector. For more details, see [5], where it is shown that for even values of the detuning parameter, all crossings are real, whereas for odd values, all crossings are avoided.

We compute the average level spacing for each symmetry sector separately, as shown in Fig. 7(a3), as a function of the detuning parameter  $\delta$ . We observe that for both symmetry sectors, the minimum values correspond to odd values of  $\delta$ , which are associated with avoided crossings, while the maximum values correspond to real crossings. This indicates a strong correlation between the two symmetry sectors.

In Fig. 7(a4), we compute the effective tunneling between the regions marked with red and blue stars for an initial coherent state in the outer region, shown in Fig. 7(a1). The results show that tunneling is significantly enhanced at parameter values where all crossings are avoided. This suggests that avoided crossings play a crucial role in facilitating quantum tunneling by allowing a smoother energy transfer between states within the same symmetry sector.

### 2. Tunneling for $\delta$ -Kerr $\xi_3$ -model

For the three-photon squeezing system, we set  $\xi_3 = 1$  and compute the spectrum of the Hamiltonian in Eq. (7) as a function of the detuning parameter, as shown in Fig. 7(a2). In this case, the Hamiltonian can be decomposed into three symmetry sectors, each represented by a different color. The spectrum displays degeneracies and exhibits both real and avoided crossings for specific values of the detuning parameter. In contrast to the two-photon squeezing case, real and avoided crossings can coexist for the same value of the detuning parameter  $\delta$ , leading to a more intricate spectral structure.

To further analyze this behavior, we compute the average level spacing for each symmetry sector separately,

as shown in Fig. 7(a3), as a function of the detuning parameter  $\delta$ . Upon closer inspection, we observe that whenever a minimum occurs in a given symmetry sector, avoided crossings appear within that sector, while real crossings occur between states belonging to different sectors. These minima alternate among the three sectors, indicating a complex interplay between the spectral properties of each symmetry sector. Additionally, we find that there is no trivial or straightforward pattern governing the locations of these minima.

*Same paragraph as  $\xi_2$ , see comment* In Fig. 7(b4), we compute the effective tunneling between regions  $O4$  and  $O5$  for an initial coherent state, shown in Fig. 7(b1). The results reveal that tunneling is enhanced at parameter values where the average level spacing reaches its minimum. This suggests that tunneling can be enhanced even when only a few avoided crossings are present and occur within a single symmetry sector.

### 3. Tunneling for $\delta$ -Kerr $\xi_4$ -model

For the four-photon squeezing system, we set  $\xi_4 = 0.25$  and compute the spectrum of the Hamiltonian in Eq. (12) as a function of the detuning parameter, as shown in Fig. 7(c2). In this case, the Hamiltonian can be decomposed into four symmetry sectors, each represented by a different color. The spectrum exhibits degeneracies and contains both real and avoided crossings for specific values of the detuning parameter. Similar to the three-photon squeezing case, real and avoided crossings can coexist for the same value of the detuning parameter  $\delta$ .

To further analyze this behavior, we compute the average level spacing for each symmetry sector separately, as shown in Fig. 7(c3), as a function of the detuning parameter  $\delta$ . We observe a strong correlation between pairs of symmetry sectors: the minima of the level spacing occurs simultaneously in two different symmetry sectors. Upon closer inspection, we find that for these values of  $\delta$ , avoided crossings appear between the correlated symmetry sectors, while real crossings occur in the other two symmetry sectors. Similarly, we find that there is no simple pattern governing the locations of these minima

In Fig. 7(c4), we calculate the effective tunneling between regions  $O5$  and  $O6$  for an initial coherent state, as depicted in Fig. 7(c1). The results indicate that tunneling is maximized at parameter values where the average level spacing is at its lowest. This suggests a strong connection between level spacing variations and the efficiency of quantum tunneling.

## V. CONCLUSION

In this work, we analyzed the quantum properties of parametric Kerr oscillators with one-, two-, three-, and four-photon squeezing, focusing on their spectral structure, symmetry sectors, and tunneling dynamics. By

studying the semiclassical Hamiltonian and characterizing its phase space, we identified the fundamental symmetries of the system and their role in quantum phase transitions.

We examined the Hamiltonian spectrum into distinct symmetry sectors, where the occurrence of real and avoided crossings depends on the detuning parameter. In the one-photon squeezing case, where only a single symmetry sector exists, all crossings are avoided. In the two-photon case, real and avoided crossings emerge in a well-defined manner, whereas in the three- and four-photon cases, they can coexist for the same detuning value, leading to a more intricate spectral structure. Additionally, we identified strong correlations between different symmetry sectors, particularly in the two- and four-photon cases, where the level spacing minima appear simultaneously in two different sectors.

By analyzing the average level spacing, we established a direct connection between spectral structure symmetry and quantum tunneling. We observed that effective tunneling is maximized at parameter values where the average level spacing reaches its minimum. This suggests that tunneling efficiency is not solely determined by the number of avoided crossings but also by their distribution across different symmetry sectors. In particular, we demonstrated that significant tunneling can occur even when avoided crossings are sparse and confined to a single symmetry sector. Furthermore, we found that symmetries can also play a protective role in tunneling

dynamics: when real crossings occur between different symmetry sectors, they can inhibit mixing between certain states, thus stabilizing the tunneling process by preventing unwanted hybridization with other energy levels.

These findings highlight the fundamental role of symmetries in the quantum dynamics of nonlinear systems and their impact on tunneling phenomena. Furthermore, they provide a systematic framework for tuning control parameters to optimize quantum tunneling, which could have important applications in experimental platforms such as superconducting circuits, polaritonic systems, and quantum optical cavities.

## ACKNOWLEDGMENTS

This project received funding through Grant No. PID2022-136228NB-C21 funded by MCIU/AEI/10.13039/501100011033 and, as appropriate, by “ERDF A way of making Europe, by ERDF/EU,” by the European Union, or by the European Union NextGenerationEU/PRTR. J.K.-R. also acknowledges support from a Spanish Ministerio de Universidades “Margarita Salas” Fellowship. Computing resources supporting this work were provided by the CEAFCM and Universidad de Huelva High Performance Computer located in the Campus Universitario “El Carmen” and funded by FEDER/MINECO Project No. UNHU-15CE-2848.

- 
- [1] J. Venkatraman, X. Xiao, R. G. Cortiñas, A. Eickbusch, and M. H. Devoret, Phys. Rev. Lett. **129**, 100601 (2022).
  - [2] N. E. Frattini, U. Vool, S. Shankar, A. Narla, K. M. Sliwa, and M. H. Devoret, Applied Physics Letters **110**, 222603 (2017), [https://pubs.aip.org/aip/apl/article-pdf/doi/10.1063/1.4984142/14500740/222603\\_1\\_online.pdf](https://pubs.aip.org/aip/apl/article-pdf/doi/10.1063/1.4984142/14500740/222603_1_online.pdf).
  - [3] N. E. Frattini, R. G. Cortiñas, J. Venkatraman, X. Xiao, Q. Su, C. U. Lei, B. J. Chapman, V. R. Joshi, S. M. Girvin, R. J. Schoelkopf, S. Puri, and M. H. Devoret, Phys. Rev. X **14**, 031040 (2024).
  - [4] J. Chávez-Carlos, T. L. M. Lezama, R. G. C. nas, J. Venkatraman, M. H. Devoret, V. S. Batista, F. Pérez-Bernal, and L. F. Santos, npj Quantum Inf. **9**, 76 (2023).
  - [5] M. A. P. Reynoso, D. J. Nader, J. Chávez-Carlos, B. E. Ordaz-Mendoza, R. G. Cortiñas, V. S. Batista, S. Lerma-Hernández, F. Pérez-Bernal, and L. F. Santos, Phys. Rev. A **108**, 033709 (2023).
  - [6] R. Dutta, D. G. A. Cabral, N. Lyu, N. P. Vu, Y. Wang, B. Allen, X. Dan, R. G. Cortiñas, P. Khazaei, M. Schäfer, A. C. C. d. Albornoz, S. E. Smart, S. Nie, M. H. Devoret, D. A. Mazziotti, P. Narang, C. Wang, J. D. Whitfield, A. K. Wilson, H. P. Hendrickson, D. A. Lidar, F. Pérez-Bernal, L. F. Santos, S. Kais, E. Geva, and V. S. Batista, J. Chem. Theory Comp. **20**, 6426 (2024), pMID: 39068594, <https://doi.org/10.1021/acs.jctc.4c00544>.
  - [7] A. C. C. de Albornoz, R. G. Cortiñas, M. Schäfer, N. E. Frattini, B. Allen, D. G. A. Cabral, P. E. Videla, P. Khazzaei, E. Geva, V. S. Batista, and M. H. Devoret, Oscillatory dissipative tunneling in an asymmetric double-well potential (2024), arXiv:2409.13113 [quant-ph].
  - [8] L. Carr, *Understanding quantum phase transitions*, Condensed Matter Physics (Taylor and Francis, Hoboken, NJ, 2010).
  - [9] F. Iachello and N. V. Zamfir, Phys. Rev. Lett. **92**, 212501 (2004).
  - [10] M. Caprio, P. Cejnar, and F. Iachello, Ann. Phys. **323**, 1106 (2008).
  - [11] P. Cejnar and P. Stránský, Phys. Rev. E **78**, 031130 (2008).
  - [12] P. Cejnar, P. Stránský, M. Macek, and M. Kloc, J. Phys. A: Math. Theor. **54**, 133001 (2021).
  - [13] L. Guo, M. Marthaler, and G. Schön, Phys. Rev. Lett. **111**, 205303 (2013).
  - [14] P. Hannaford and K. Sacha, APPS Bull. **32**, 12 (2022).
  - [15] J. von Neumann and E. Wigner, Phys. Z. **30**, 467 (1929).
  - [16] Y. Demkov and P. Kurasov, Theoretical and Mathematical Physics **153**, 1407 (2007).
  - [17] M. C. M. C. Gutzwiller, *Chaos in classical and quantum mechanics* (Springer-Verlag, New York, 1990).

## Appendix A: Classical limit

To derive a classical Hamiltonian applicable to any set of control parameters, and to approximate a continuous spectrum even for fixed values of the control parameter that are not necessarily large, we introduce the parameter  $N_{eff}$ . The reciprocal of  $N_{eff}$  quantifies the size of the zero-point fluctuations. We express this as:

$$\hat{a} = \sqrt{\frac{N_{eff}}{2}}(\hat{q} + i\hat{p}), \quad [\hat{q}, \hat{p}] = \frac{i}{N_{eff}} \quad (\text{A1})$$

The classical limit is achieved by taking  $N_{eff} \rightarrow \infty$ , as this ensures the transition to a continuous spectrum. In this regime, the quantum Hamiltonian gradually transforms into its classical counterpart, since  $\hat{q} \rightarrow q$  and  $\hat{p} \rightarrow p$ . Apply to eq. 1, the quantum Hamiltonian

$$\begin{aligned} \hat{H}_\mu &= -\frac{\delta N_{eff}}{2}(\hat{q} + i\hat{p})^2 + \frac{N_{eff}^2}{4}(\hat{q} + i\hat{p})^2(\hat{q} + i\hat{p})^2 \\ &\quad - \frac{\xi_\mu N_{eff}^{\mu/2}}{2^{\mu/2}} [(\hat{q} + i\hat{p})^2 + (\hat{q} + i\hat{p})^2] \end{aligned} \quad (\text{A2})$$

leads to the classical Hamiltonian

$$\frac{H_\mu^c}{\hbar K N_{eff}^2} = -\frac{\delta^c}{2}(q^2 + p^2) + \frac{1}{4}(q^2 + p^2)^2 - \frac{2\xi_\mu^c}{2^{\mu/2}} \mathcal{F}_\mu, \quad (\text{A3})$$

the classical control can be mapped back to their counterparts in the quantum Hamiltonian through the transformation given by: where  $\delta^c = \delta/N_{eff}$ ,  $\xi_\mu^c = \xi_\mu/N_{eff}^{2-\mu/2}$  and  $\mathcal{F}_\mu$  is defined as  $\text{Re}[(q + ip)^\mu]$ . In the main text, we have fixed  $N_{eff} = 1$

## Appendix B: Order parameter of quantum phase transition

The order of the transitions, as discussed in the main text, can be directly examined using the definition of the order parameter. In our case, the order parameter is given by the derivative of the ground state energy with respect to the relevant parameter:  $\delta$  for transitions along the y-axis and  $\xi_\mu$  for transitions along the x-axis in parameter space.

In Fig.8, we illustrate the universal procedure for intensifying the order of the transition by analyzing taking two different QPTs associated with  $\xi_2$ . Straight lines in parameter space are chosen to study transitions between region I and II (dependent on  $\xi_2$ ), and III and  $\tilde{III}$  (dependent on  $\delta$ ).

The upper panel of Fig.8 present the GS energy obtained from quantum (classical) calculations, shown in blue (red). By leveraging fixed points analysis, we can determine the GS  $(q, p)$  coordinates. For instance, in region I, the GS is located at  $(0, 0)$ . As  $\xi_2$  increases, this point becomes unstable, marking the transition in region

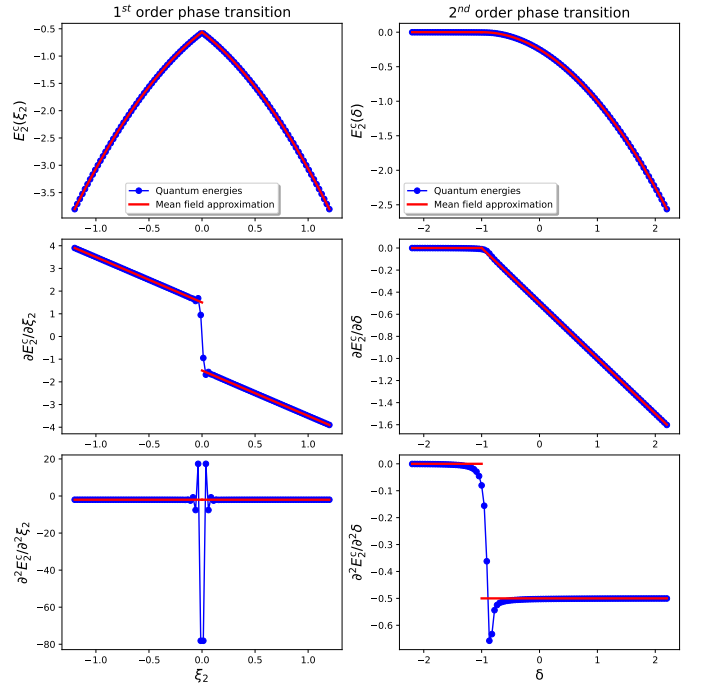


FIG. 8. General determination of the transition order. The blue lines and dots (red lines) are the quantum (classical) calculation, as explained in B. (a) GS energies and their derivatives along a constant  $\delta = 1.5$ , illustrating a first-order transition. (b) Transition along  $\xi_2 = 0.5$ , exhibiting a second-order phase transition. For both cases,  $N = 2000$  for each parity, and  $N_{eff} = 100$  ensures that the quantum and classical systems remain close to one another.

**II.** Overall, the classical curves correspond to the energies from 9, with their derivatives with respect to  $\delta$  or  $\xi_2$ .

In Fig.8 left panels, a horizontal line in parameter space is taken for  $\delta = 1.5$ , revealing a first order phase transition characterized by a discontinuity in the order parameter (middle panel). Conversely, in the right panels of Fig.8, a vertical line for  $\xi_2 = 0.5$  indicates a second order transition (lower panel). This methodology can be systematically applied to any QPT across different cases.

## Appendix C: When the transition is only classical

Under certain control parameter regimes, some quantum phase transitions may not be directly observable through quantum Hamiltonian diagonalization, even when semiclassical analysis predicts their presence. This effect is particularly evident in Case II of the  $\delta$ -Kerr  $\xi_3$  model. For small parameter values, the transition is suppressed and remains undetectable, as illustrated in Fig.9(a). However, as the parameters increase, the transition—specifically the ESQPT—becomes clearly visible, as shown in Fig.9(b).

This phenomenon highlights the subtle interplay be-

tween system parameters and the detectability of quantum phase transitions. It underscores the fact that while semiclassical methods can predict the existence of a transition, the quantum manifestation of such transitions may be obscured for certain parameter regimes. The eventual emergence of the ESQPT at higher parameter values suggests that the critical features associated with these transitions become more pronounced as the system moves deeper into the semiclassical limit. This observation emphasizes the necessity of a comprehensive exploration of the parameter space, leveraging both semiclassical approximations and exact quantum diagonalization, to fully characterize the rich dynamical and spectral properties of the system.

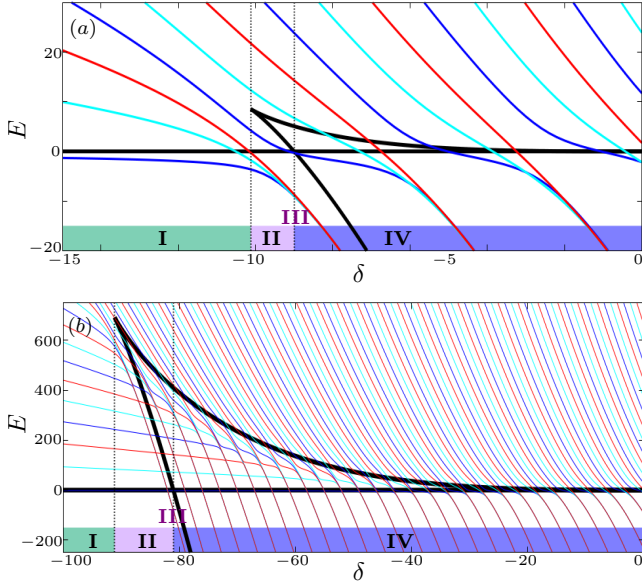


FIG. 9. Energy as a function of the squeezing parameter  $\delta$  for (a)  $\xi_3 = 3$  and (b)  $\xi_3 = 9$ . Both panels illustrate the transition pathway from case 3.I to case 3.IV, passing through intermediate cases 3.II and 3.III. The black lines represent the classical energy of the equilibrium points. In the strongly quantum regime (a), the ESQPT predicted by the classical description from 3.II to 3.III remain undetectable due to quantum effects. By increasing the system parameters, as shown in panel (b), these transitions become more apparent, aligning more closely with the semiclassical predictions.